

Guo Jessica Sijia (Orcid ID: 0000-0002-9566-9182)
Smith William (Orcid ID: 0000-0002-5785-6489)

Dynamic regulation of water potential in *Juniperus osteosperma* mediates ecosystem carbon fluxes

Jessica S. Guo^{1,*}, Mallory L. Barnes², William K. Smith³, William R.L. Anderegg⁴, Steven A. Kannenberg^{5,6}

¹ Arizona Experiment Station, University of Arizona, Tucson, Arizona, 85721, USA

² O'Neill School of Public and Environmental Affairs, Indiana University, Bloomington, Indiana, 47405, USA

³ School of Natural Resources and the Environment, University of Arizona, Tucson, Arizona, 85721, USA

⁴ School of Biological Sciences and Wilkes Center for Climate Science and Policy, University of Utah, Salt Lake City, Utah, 84112, USA

⁵ Department of Biology and Graduate Degree Program in Ecology, Colorado State University, Fort Collins, Colorado, 805023, USA

⁶ Department of Biology, West Virginia University, Morgantown, West Virginia, 26506, USA

* Correspondence: [Jessica S. Guo <jessicaguo@arizona.edu>](mailto:jessicaguo@arizona.edu)

ORCIDs: JSG (0000-0002-9566-9182), MLB (0000-0001-8528-6981), WKS (0000-0002-5785-6489), WRLA (0000-0001-6551-3331), SAK (0000-0002-4097-9140)

Summary

- Some plants exhibit dynamic hydraulic regulation, in which the strictness of hydraulic regulation (i.e., iso/anisohydry) changes in response to environmental conditions. However, the environmental controls over iso/anisohydry and the implications of flexible hydraulic regulation for plant productivity remain unknown.
- In *Juniperus osteosperma*, a drought-resistant dryland conifer, we collected a 5-month growing season timeseries of *in situ*, high temporal-resolution plant water potential (Ψ) and stand gross primary productivity (GPP). We quantified the stringency of hydraulic

This is the author manuscript accepted for publication and has undergone full peer review but has not been through the copyediting, typesetting, pagination and proofreading process, which may lead to differences between this version and the Version of Record. Please cite this article as doi: [10.1111/nph.19805](https://doi.org/10.1111/nph.19805)

regulation associated with environmental covariates and evaluated how predawn water potential contributes to empirically predicting carbon uptake.

- *J. osteosperma* showed less stringent hydraulic regulation (more anisohydric) after monsoon precipitation pulses, when soil moisture and atmospheric demand were high, and corresponded with GPP pulses. Predawn water potential matched the timing of GPP fluxes and improved estimates of GPP more strongly than soil and/or atmospheric moisture, notably resolving GPP underestimation prior to vegetation green-up.
- Flexible hydraulic regulation appears to allow *J. osteosperma* to prolong soil water extraction and therefore the period of high carbon uptake following monsoon precipitation pulses. Water potential and its dynamic regulation may account for why process-based and empirical models commonly underestimate the magnitude and temporal variability of dryland GPP.

Keywords: carbon uptake, dryland ecosystem, hydraulic regulation, juniper woodland, iso/anisohydry, precipitation pulse dynamics, stem water potential

Introduction

Along the soil-plant-atmosphere continuum, gradients of water potential (Ψ) drive water transport and govern the tradeoff between obtaining carbon dioxide for photosynthesis and water loss through stomata (Berry *et al.*, 2010). The concept of a ‘plant water use strategy’ encompasses the numerous ways plants have evolved to confront this inescapable dilemma, including the prevalent iso/anisohydry spectrum based on the stomatal regulation of Ψ (Jones, 1998; Tardieu & Simonneau, 1998). Isohydry describes a conservative stomatal strategy to minimize reductions in Ψ and preserve hydraulic conductivity, while anisohydry is a profligate stomatal strategy that prioritizes carbon gain at the expense of low Ψ . The degree of iso/anisohydry describes plant strategy in response to declining soil moisture absent other limiting factors (Novick *et al.*, 2019) and is generally operationalized as a species-level and theoretical trait. However, recent work has demonstrated that these strategies can be quite variable within a species and may arise from plant-environment interactions (Hochberg *et al.*, 2018), including vapor pressure deficit (VPD), which is often decoupled from soil moisture at short timescales (Novick *et al.*, 2016). Within-species shifts in iso/anisohydry have been observed for *Larrea tridentata* (Guo *et al.*, 2020) and *Quercus douglasii* (Feng *et al.*, 2019) during different seasons, in *Quercus suber* in response to competition (Haberstroh *et al.*, 2022), *Acacia aptaneura* as a result of repeated experimental drought (Nolan *et al.*, 2017), and in multiple species between wet and dry years (Wu *et al.*, 2021).

The implications of temporally-variable hydraulic strategies on ecosystem carbon (C) fluxes have not been fully elucidated. This knowledge gap may limit accurate modeling of carbon and water cycle dynamics, which in turn restricts our ability to predict and mitigate climate change impacts (Kennedy *et al.*, 2019a; Novick *et al.*, 2022). Particularly in dryland ecosystems, persistent water limitation and episodic precipitation promote tight coupling between carbon and water cycles (Biederman *et al.*, 2016), resulting in added temporal complexity that can be difficult to model (Noy-Meir, 1973; Loik *et al.*, 2004; Ogle & Reynolds, 2004; Feldman *et al.*, 2018). Dryland ecosystems are largely responsible for the interannual variability of the global carbon sink (Poulter *et al.*, 2014; Ahlström *et al.*, 2015), yet dynamic global vegetation models have been found to significantly underestimate the interannual variability of C uptake in dryland regions (Biederman *et al.*, 2017; MacBean *et al.*, 2021a). Understanding the temporal dynamics

and environmental sensitivity of plant hydraulic strategies may be critical to improving predictive forecasts of the global carbon cycle (Eller *et al.*, 2020; Sabot *et al.*, 2020, 2022).

Despite its importance, plant hydraulic stress is often notably absent from large-scale estimates of ecosystem productivity (Smith *et al.*, 2019). Such models commonly combine remotely-sensed indices of vegetation greenness and light use efficiency [LUE; Running *et al.* (2004); Zeng *et al.* (2022)], defined as the slope of the relationship between biomass and cumulative intercepted photosynthetically active radiation (Monteith *et al.*, 1977). Greenness indices can represent the structural capacity for photosynthesis on a seasonal basis (Wang *et al.*, 2022), but do not capture the sub-daily constraints imposed by soil and atmospheric drought, such that productivity seasonality is much weaker in remotely-sensed than tower-based fluxes (Garbulsky *et al.*, 2008; Biederman *et al.*, 2017; Smith *et al.*, 2019; Pierrat *et al.*, 2021). Instead, water stress effects are typically incorporated into estimates of LUE using moisture scalars derived from estimates of VPD [e.g., MODIS LUE; Zhao & Running (2010)], remotely sensed vegetation or evaporative indices [e.g., eddy covariance; (EC)-LUE model Yuan *et al.* (2007)], or combined VPD and soil moisture [e.g., CFLUX; King *et al.* (2011)]. However, the range of ecophysiological responses to moisture stress are too complex for a single environmentally-derived indicator or function to adequately represent (Zhang *et al.*, 2015). Plant water potential, a direct metric of plant water stress that integrates soil and atmospheric drivers, may thus provide a key physiological constraint on ecosystem productivity, which could improve our ability to represent drought impacts and quantify interannual variability of C uptake.

Pinyon-juniper woodlands are broadly distributed in the southwestern United States and provide a well-studied test system for how hydraulic strategies like iso/anisohydry can modulate productivity and mortality (McDowell *et al.*, 2008). Pinyon mortality following the 2002-2003 drought was likely associated with differences in plant hydraulic regulation (Breshears *et al.*, 2009; Plaut *et al.*, 2012); juniper survival was largely attributed to a less hydraulically vulnerable xylem and thus a greater ability to withstand low water potentials (McDowell *et al.*, 2008). Although generally considered anisohydric, *Juniperus monosperma* exhibited strong stomatal control and negligible xylem embolism under drought manipulation (Garcia-Forner *et al.*, 2016b), thereby challenging the hypothesis that anisohydric species are more prone to hydraulic failure. As the southwestern US megadrought persists (Williams *et al.*, 2022) and induces

mortality even among resilient *Juniperus* spp. (Kannenberg *et al.*, 2021), it is imperative to examine how flexible hydraulic strategies interact with plant productivity and survival.

In this study, we utilize a five-month time-series of plant Ψ and gross primary productivity (GPP) in a juniper woodland to evaluate the temporal dynamics of hydraulic strategy and incorporate plant water stress into a common GPP framework. Previous work by Guo *et al.* (2020) examined dynamic hydraulic strategy in *Larrea tridentata* but lacked a co-located timeseries of ecosystem carbon fluxes. By contemporaneously measuring plant Ψ and GPP continuously at daily resolution, we can directly investigate the implications of Ψ regulation and hydraulic status for productivity in an iconic southwestern species. We ask:

- 1) Does plant hydraulic regulation vary over time in *J. osteosperma*?
- 2) How are temporal patterns in hydraulic regulation related to GPP over a growing season?
- 3) Can GPP prediction be enhanced by plant water potential?

Materials and Methods

This study was conducted at an early-successional pinyon-juniper woodland (37.5241 N, 109.7471 W, 1866 m a.s.l.) in southeastern Utah. Local climate conditions include cold winters and hot, dry summers, with high interannual variability in summer precipitation due to its location at the northern boundary of the North American Monsoon. The locally flat topography is dominated by Utah juniper (*Juniperus osteosperma* (Torr.) Little, 92% tree basal area) and two-needle pinyon (*Pinus edulis* Engelm., 8% tree basal area), with sparse understory comprising big sagebrush (*Artemisia tridentata* Nutt.), prickly pear cactus (*Opuntia* spp.), and bunchgrasses. Mean growing season leaf area index was 0.4, and the site was chained in the 1960s, resulting in a relatively even-aged and sized population of *J. osteosperma*. See Kannenberg *et al.* (2023) for further site description and processing of eddy covariance variables.

Plant water potential

Stem water potential of seven mature *J. osteosperma* within the tower footprint (< 20 m) was monitored with both automated and manual measurements between May 24 and November 5, 2021. Half-hourly water potential was monitored with stem psychrometers (ICT International PSY1) calibrated prior to installation. Two instruments per tree were installed by removing the

bark and phloem to expose a flat xylem surface. Psychrometer sensor heads were attached with self-adhesive silicone tape to maintain a tight seal and wrapped in reflective insulation to minimize temperature gradients. Because plant wounding responses can fill the sensor chamber, each psychrometer was uninstalled, cleaned with chloroform, and reinstalled on a new branch every 4-5 weeks. The day after reinstallation, the xylem water potential was measured manually with a Scholander-type pressure chamber (PMS 610) by excising a needle cluster with diameter between 2 and 4 mm and measuring within 2 minutes of collection; psychrometer water potentials generally matched pressure chamber values (Kannenberg *et al.*, 2023).

The half-hourly stem water potential time series were subjected to quality control by visual assessment and aggregated to daily values. After removing data during the maintenance period (+ 1 day) and outliers that were > 0.5 MPa from adjacent points, data that met the following criteria were also discarded: 1) a step change in the magnitude of water potential not attributable to a precipitation event; 2) loss of diurnal pattern in water potential. On average, data from 10 out of 14 psychrometers were available during a given period. Half-hourly stem water potential was summarized to predawn (Ψ_{PD} , 2 hours prior to sunrise) and midday (Ψ_{MD} , 2 hours following solar noon) for each logger. In addition, site-level means of predawn and midday water potential were calculated and missing values (10 and 8, respectively) were imputed using Kalman Smoothing via the R package ‘imputeTS’ (Moritz & Bartz-Beielstein, 2017).

Vegetation indices and fAPAR

We adopted a Monteith light use efficiency framework (Monteith, 1972) to estimate plant productivity. This framework conceptualizes GPP as the product of absorbed photosynthetically active radiation (APAR) and the efficiency with which light is converted to fixed carbon (LUE). APAR is represented as a product of photosynthetically active radiation (PAR) and the fraction of PAR absorbed by plant canopies (fAPAR). The foundational equation from Monteith’s framework can be expressed as:

$$GPP = LUE \cdot PAR \cdot fAPAR \quad (1)$$

Many current models for estimating GPP are grounded in this framework or its variations. Here, we used the the near-infrared reflectance of vegetation index (NIRv Badgley *et al.*, 2017, 2019)

as a proxy for fAPAR. This choice was informed by the strong correlation between NIRv and modeled fAPAR across various soil reflectances and its robustness at low vegetation cover (Badgley *et al.*, 2017; Wang *et al.*, 2022).

We calculated NIRv from Moderate Resolution Imaging Spectroradiometer (MODIS) nadir bidirectional reflectance distribution function adjusted daily reflectance product (MCD43A, 1 d, 500 m, collection 6.1) using the point extraction tool AppEARS. MODIS bands 1 (620-670 nm) and 2 (841-876 nm) were combined with background soil reflectance of 0.08 to represent NIRv following Badgley *et al.* (2017). The pixel containing the coordinates of US-CdM was filtered to include only the highest quality observations (MODIS quality flag = 0). Resulting values were smoothed using a Savitzky-Golay filter of derivative order 0, filter order 3, and window length 5.

Model description - hydraulic regulation

To specify the hydraulic regulation model, we used the Martinez-Vilalta *et al.* (2014) equation to relate Ψ_{MD} to Ψ_{PD} :

$$\Psi_{MD} = \sigma \cdot \Psi_{PD} + \lambda \quad (2)$$

where σ represents the stringency of hydraulic regulation and λ describes the pressure drop when soil moisture is not limiting. Plant hydraulic regulation can be described as isohydry if $\sigma < 1$, anisohydry if $\sigma \approx 1$, and extreme anisohydry if $\sigma > 1$ (Martínez-Vilalta *et al.*, 2014).

To allow hydraulic regulation and GPP to vary over the growing season, we specified a hierarchical Bayesian model similar to Guo *et al.* (2020), which estimated σ and λ as linear functions of environmental drivers. Here, we used maximum daily VPD (D) and volumetric soil water content at 10 cm (W_{10}), which had the highest correlation with plant Ψ and GPP (Kannenberg *et al.*, 2023). Furthermore, we implemented the stochastic antecedent model (Ogle *et al.*, 2015) to quantify the influence of past environmental conditions. The data model for hydraulic regulation describes the likelihood of each observed Ψ_{MD} , which was normally distributed for each observation i ($i = 1, 2, \dots, 1425$):

$$\Psi_{MD_i} \sim \text{Normal}(\hat{\Psi}_{MD_i}, \sigma_{\Psi}^2) \quad (3)$$

where $\hat{\Psi}_{MD_i}$ is the predicted or mean midday water potential and $\sigma_{\hat{\Psi}}^2$ represents the observation variance. $\hat{\Psi}_{MD_i}$ was modeled according to Eqn. 3, where all terms were allowed to vary over time, either as direct observations (Ψ_{MD}, Ψ_{PD}) or as modeled parameters (σ, λ). The time-varying estimates of hydraulic regulation, σ and λ were indexed by i and modeled as linear combinations of two antecedent covariates and their interaction:

$$\begin{aligned}\sigma_i &= \beta_0 + \beta_1 \cdot D_i^{ant} + \beta_2 \cdot W_{10_i}^{ant} + \beta_3 \cdot D_i^{ant} \cdot W_{10_i}^{ant} + \varepsilon_{\sigma,t(i)} \\ \lambda_i &= \alpha_0 + \alpha_1 \cdot D_i^{ant} + \alpha_2 \cdot W_{10_i}^{ant} + \alpha_3 \cdot D_i^{ant} \cdot W_{10_i}^{ant} + \varepsilon_{\lambda,t(i)}\end{aligned}\quad (4)$$

The β and α parameters were estimated for all trees. ε_{σ} and ε_{λ} represent the random effects of each tree, where $t(i)$ indicates tree t associated with each observation i . D_{max} and W_{10} were scaled using the 2021 mean and standard deviation so that regression coefficients could be compared and β_0 and α_0 could be interpreted as σ and λ , respectively, under mean environmental conditions. Antecedent VPD (D^{ant}) and soil water content (W_{10}^{ant}) were constructed using daily time series of each scaled environmental variable (Ogle *et al.*, 2015):

$$\begin{aligned}D_i^{ant} &= \sum_{p=0}^{T_{lag}} \omega_{D_p} \cdot D_{t(i)-p} \\ W_{10_i}^{ant} &= \sum_{p=0}^{T_{lag}} \omega_{W_p} \cdot W_{t(i)-p}\end{aligned}\quad (5)$$

where p indicates the time step, T_{lag} represents the total number of past time-steps considered, ω_{D_p} and ω_{W_p} indicates the weight or relative importance of the p th time step into the past, and $D_{t(i)-p}$ and $W_{t(i)-p}$ are the observed value of each variable at p time steps ago. Antecedent covariates are weighted averages of past covariate values, where the weights are stochastically determined by the data. Here, D^{ant} was constructed using daily values from the current day to 4 days ago ($p = 1, T_{lag} = 5$), while W_{10}^{ant} was constructed using three-day averages of W_{10} from the current day to 20 days ago ($p = 3, T_{lag} = 7$).

To complete this model, a zero-centered hierarchical normal prior was specified for tree random effects:

$$\begin{aligned}\mathcal{E}_{\sigma,t} &\sim \text{Normal}(0, \sigma_{\sigma}^2) \\ \mathcal{E}_{\lambda,t} &\sim \text{Normal}(0, \sigma_{\lambda}^2)\end{aligned}\quad (6)$$

where reparameterization by sweeping was employed to ensure identifiability between the intercepts (β_0, α_0) and the random effects (Vines *et al.*, 1996).

All remaining parameters were given standard priors following Gelman *et al.* (2014). The regression coefficients were assigned relatively non-informative normal priors centered at zero with large variance. Antecedent importance weights, vectors of length T_{lag} (Eqn. 5), were given non-informative Dirichlet priors that assume *a priori* that each past time step has equal importance, and that constrain weights for each covariate to sum to 1 across all time steps, p . The standard deviation of tree random effects (σ_{σ} and σ_{λ}) were given relatively non-informative *Uniform*(0,1) priors, while the measurement error precision ($1/\sigma_{\psi}^2$) was assigned a conjugate, relatively non-informative *Gamma*(0.1,0.1) prior.

Model description - GPP

To assess the drivers of daily ecosystem productivity, we developed a two-part model based on the Monteith (1972) framework. In this model, daily GPP was modeled sequentially, first as a function of NIRv and incoming PAR. The residuals of this model were considered indicative of variation in LUE.

Typically, LUE is conceptualized as the product of its theoretical maximum (LUE_0) and a function of environmental stressors that reduce optimal light-use efficiency. Given that LUE_0 is a theoretical construct assumed to remain constant within our study (e.g., within a season), the GPP model residuals can be interpreted as 1) impacts of environmental stressors on LUE and 2) random noise or uncertainty inherent in the data. Thus, while we evaluated GPP model residuals as functions of water stress indicators, including VPD, soil moisture, and predawn water potential, we also acknowledge that they include data uncertainty and random noise.

The likelihood of observed *GPP* was normally distributed for each observation j ($j = 1, 2, \dots, 166$):

$$GPP_j \sim \text{Normal}(\widehat{GPP}_j, \sigma_{GPP}^2) \quad (7)$$

where \widehat{GPP}_j is the predicted or mean daily GPP and the variance σ_{GPP}^2 represents the uncertainty in observed GPP . \widehat{GPP}_j was modeled as a linear function of $NIRv$, PAR , and their interaction, representing the photosynthetic-capacity component of the Monteith (1972) formulation.

$$\widehat{GPP}_j = \gamma_0 + \gamma_1 \cdot NIRv_j + \gamma_2 \cdot PAR_j + \gamma_3 \cdot NIRv_j \cdot PAR_j \quad (8)$$

All remaining parameters were given standard priors as previously described.

To interpret the remaining GPP as *LUE*, we calculated the residuals of the above model as the posterior mean of $GPP_j - \widehat{GPP}_j$; residuals were scaled for improved model mixing. The likelihood of the residual model described scaled *resid* as normally distributed for observations k ($k = 1, 2, \dots, 166$):

$$resid_k \sim Normal(\widehat{resid}_k, \sigma_{resid}^2) \quad (9)$$

where \widehat{resid}_k is the predicted residual between observed and modeled (Eqn. 7, Eqn. 8) GPP, and the variance σ_{resid}^2 represents the uncertainty in observed *resid*. \widehat{resid}_k is interpreted as a dynamic *LUE* constraint on GPP after vegetation greenness and light interception is accounted for. We devised three *LUE* formulations that account for the combined impact of concurrent VPD and antecedent soil moisture (Eqn. 10), antecedent soil moisture alone (Eqn. 11), and concurrent predawn water potential (Eqn. 12):

$$\widehat{resid}_k = \delta_0 + \delta_1 \cdot D_{max_k} + \delta_2 \cdot W_{10_k}^{ant} + \delta_3 \cdot D_{max_k} \cdot W_{10_k}^{ant} \quad (10)$$

$$\widehat{resid}_k = \eta_0 + \eta_1 \cdot W_{10_k}^{ant} \quad (11)$$

$$\widehat{resid}_k = \theta_0 + \theta_1 \cdot \overline{\Psi_{PD}_k} \quad (12)$$

where $\overline{\Psi_{PD}}$ were the gapfilled means of predawn water potential at the site level. Antecedent weights for W_{10}^{ant} were constructed identically to Eqn. 5, with unique weights determined by the GPP residuals.

Model implementation and interpretation

The above models were implemented in JAGS 4.3.0 (Plummer, 2003) using R 4.1.1 and ‘rjags’ 4.13 (R Core Team, 2021; Plummer, 2022). For each model, three parallel Markov chain Monte Carlo sequences were initiated with dispersed starting values; initial iterations were run until model convergence, as indicated by the Gelman and Rubin (Gelman & Rubin, 1992) statistic. Models were then run for 150,000 iterations and thinned by 50 to reduce within-chain autocorrelation and storage requirements, yielding a total of 9000 relatively independent posterior samples for each quantity of interest, including the regression coefficients and antecedent weights. Posterior distributions were summarized by their means and 95% highest posterior density credible intervals (henceforth, 95% CIs). Covariate effects were significant if the 95% CI did not overlap zero. To quantify seasonal variation in σ , the posterior samples of the β regression coefficients and antecedent weights were combined with the time-series of scaled D_{max} and W_{10} to produce posterior means and 95% CIs. Model comparison criteria for the three forms of GPP residual models included posterior predictive loss (Gelfand & Ghosh, 1998) and the coefficient of determination (R^2) between observed and predicted values.

Results

Seasonal dynamics of Ψ , GPP, and σ

Predawn (Ψ_{PD}) and midday (Ψ_{MD}) stem water potentials responded dynamically to moisture inputs, particularly during the monsoon period (Fig. 1). Monsoon onset, determined as the day on which on the 10% of the total July, August, and September precipitation was accumulated (Grantz *et al.*, 2007), occurred on 2021-07-23. Prior to monsoon onset, the generally high VPD and low soil moisture yielded relatively consistent mean Ψ_{PD} between -2 and -4 MPa. During the monsoon period, VPD and soil moisture were less extreme than during the more arid mid-summer period, though highly variable as a result of three major pulse-drydown events (Fig. 1). Beginning with the first major pulse event (39 mm on 2021-07-27), mean Ψ_{PD} remained above -2 MPa continuously for 46 days; however, minimum mean Ψ_{PD} was similar in premonsoon and monsoon periods due to rapid decline in Ψ_{PD} following the third major pulse-drydown. Finally, mean Ψ_{PD} stayed above -2 MPa during the fall season, likely due to cooling temperatures and reduced atmospheric demand.

Seasonal GPP dynamics were similarly responsive to precipitation inputs (Fig. 1b). GPP declined during the premonsoon period to near-zero levels, while the onset of the monsoon prompted sharp increases. Interestingly, while the first major pulse event was the largest single-day total (39 mm on 2021-07-27) that corresponded to almost immediate increases in Ψ_{PD} , GPP rose only modestly. All three peaks in GPP during the monsoon period lagged the moisture inputs and lasted more briefly than peaks in Ψ_{PD} (Fig. 1). Fall GPP averaged $0.1 \text{ mol CO}_2 \text{ m}^{-2} \text{ d}^{-1}$, about the same as initial GPP during the premonsoon period.

The dynamics of hydraulic regulation can be visually estimated by plotting stem Ψ_{MD} and Ψ_{PD} for each season (Fig. 2). The slope σ appeared similar during the premonsoon and fall periods, although W and therefore stem Ψ differed substantially between the two seasons. During the monsoon period, two slopes were detected via segmented regression, with $\sigma > 1$ occurring when soil moisture was high and $\Psi_{PD} > -0.6 \text{ MPa}$; the same region during the fall season had a much shallower slope.

Environmental drivers and timescales of σ

The hydraulic regulation model (Eqn. 3 - Eqn. 6) fit the data very well (Fig. S1, observed vs. predicted Ψ_{MD} $R^2 = 0.920$) with low bias (slope of observed vs. predicted = 0.919).

Temporal variation in hydraulic regulation (σ) was strongly positively associated with antecedent VPD (D^{ant}), antecedent soil water content (W_{10}^{ant}), and their interaction (Fig. 3a), indicating that *J. osteosperma* became especially anisohydric under dry atmospheric conditions when soils were wet. While the positive effect of D was primarily driven by the atmospheric dryness on the same day, soil moisture up to 11 days prior was influential (Fig. 3b). The pressure drop parameter λ was negatively associated with the interaction of D^{ant} and W_{10}^{ant} , although the main effects were not significant (Fig. 3a).

Temporal patterns in σ and GPP

Although general trends in hydraulic regulation can be inferred from grouping Ψ_{MD} and Ψ_{PD} by season (e.g., Fig. 2), the hierarchical Bayesian model permitted combining posterior parameter distributions with environmental covariates to produce daily timeseries of predicted σ (e.g.,

Fig. 4a), which cannot be determined empirically. During the premonsoon, *J. osteosperma* shifted between iso- and anisohydry, with σ values near 1. But during the monsoon season, the three main pulse events heralded peaks in σ that signify extreme anisohydry, with σ values well above 1, driven by the high VPD and still-wet soils that characterize the post-precipitation period. Finally, in the fall, *J. osteosperma* returned to isohydry, and σ fell below 1.

The trends in daily σ corresponded well to observed time-series of GPP (Fig. 4a), particularly in the responsiveness of both σ and GPP to the three main pulse events. Thus, σ and GPP were positively correlated during the monsoon period ($r = 0.653, p < 0.001$, Fig. 4b). However, the peak in GPP appeared to lead the peak in σ , as the highest Pearson's correlation between GPP and σ was achieved at a 1-2 day offset between the two timeseries (Fig. 4c).

Plant water potential relationship to GPP

The initial GPP model (Eqn. 7, Eqn. 8) also fit the data well (Fig. 5c, observed vs. predicted $GPP R^2 = 0.733$), although with some degree of bias (slope of observed vs. predicted = 0.732) such that some high GPP values were underpredicted. Comparing the GPP and NIRv time series (Fig. 5a), the first major pulse event elicited a strong GPP response prior to any green up detected optically by NIRv. Conversely, low, near-zero GPP in mid to late July was not matched by extreme lows in scaled PAR or NIRv, resulting in overprediction of low GPP values. GPP was positively associated with NIRv and the interaction between NIRv and PAR (Fig. 5b), though PAR alone was not significantly associated with GPP.

Residuals from the initial GPP model were interpreted as fluctuations in light use efficiency (LUE), and model fit was compare among three functional forms: environmental covariates with D and W_{10}^{ant} (Eqn. 5, Eqn. 10), soil water content with W_{10}^{ant} only (Eqn. 5, Eqn. 11), and predawn water potential with $\overline{\Psi_{PD}}$ only (Eqn. 12). Of the three models, the $\overline{\Psi_{PD}}$ model had the fewest effective number of parameters (pD), lowest posterior predictive loss ($D\infty$), strongest coefficient of determination (R^2), and lowest bias (Fig. 6b,c).

Among the LUE models, the $\overline{\Psi_{PD}}$ fit the GPP residuals modestly well (observed vs. predicted $resid\ R^2 = 0.199$) while minimizing posterior predictive loss (Fig. 6b). Combining the initial

GPP model and the best-performing LUE model using $\overline{\Psi_{PD}}$ improved the overall R^2 from 0.733 to 0.800 and substantially reduced bias from 0.732 to 0.89 (Fig. 5c, Fig. 6c).

The strong performance of $\overline{\Psi_{PD}}$ for predicting GPP residuals is likely due to their close temporal coherence (Fig. 6a), which outperformed models with W_{10}^{ant} alone or in conjunction with D (Fig. 6b). The antecedent weights for W_{10}^{ant} (Fig. S2) indicated that GPP residuals lagged soil moisture by 3-5 days, but the temporally-weighted soil moisture still did not correlate as strongly with GPP residuals as $\overline{\Psi_{PD}}$ did. Surprisingly, neither D nor W_{10}^{ant} was significantly associated with the GPP residuals in the environmental covariates model (Fig. 6b), perhaps because D and PAR were highly correlated (Fig. 1) and the initial GPP model already accounted for PAR.

Discussion

In this study, we aimed to improve our understanding of temporal variability in plant hydraulic regulation and its relationship to ecosystem carbon uptake. We leveraged contemporaneous, high-resolution water potential and carbon flux data to compare temporal trends in daily plant water potential, hydraulic behavior, and GPP in a juniper woodland. First, we found that in *J. osteosperma*, hydraulic regulation varied over the growing season. Increasing anisohydricity was observed following precipitation pulses, associated with high soil moisture and high atmospheric demand (Fig. 3). Next, we found that GPP and σ were most positively correlated during the monsoon season, but with different temporal trajectories following precipitation pulses (Fig. 4). Surprisingly, although both Ψ_{MD} and Ψ_{PD} responded rapidly to precipitation inputs, plants achieved maximum σ 1-2 days after peak GPP was reached for a given moisture pulse (Fig. 4c). Together, these results hint at the intriguing possibility that extreme anisohydry can serve to maximize soil water extraction and prolong GPP pulses in dryland ecosystems. Finally, predawn water potential explained more variability in GPP compared to environmental covariates associated with atmospheric and soil moisture conditions (Fig. 6). As a direct metric of water stress, plant water potential closely matched the timing of GPP variability not accounted for by light availability and vegetation greenness, underscoring water stress as the dominant constraint on intra-annual GPP dynamics in dryland ecosystems.

Temporally-varying hydraulic behavior

Juniperus species are considered more anisohydric than co-occurring pinyon pines due to their more cavitation-resistant xylem (Linton *et al.*, 1998), higher hydraulic safety margins (Plaut *et al.*, 2012), and lower leaf water potentials (West *et al.*, 2007; Breshears *et al.*, 2009), while their categorization based on stomatal control is less conclusive (Garcia-Forner *et al.*, 2016a). Due to less vulnerable xylem in *Juniperus*, low water potentials alone do not suggest less stringent stomatal control, as they must be interpreted relative to vulnerability curve parameters such as Ψ_{50} , or the xylem pressure at 50% loss of hydraulic conductance. Here, a 166-day time series of Ψ_{PD} and Ψ_{MD} in *J. osteosperma* reveals strong, context-dependent variation in hydraulic regulation, an intermediate timescale that can potentially bridge the gap between short-term stomatal response-based definition of iso/anisohydry (Tardieu & Simonneau, 1998) and definitions that rely on seasonal extremes (Klein, 2014; Martínez-Vilalta *et al.*, 2021). We posit that response-based metrics (Kannenberg *et al.*, 2022) can be used to quantify plant water use strategies without distinguishing between active versus passive regulation, yet can enhance predictive understanding of plant-environment interactions.

Dry air in combination with wet soil drove large increases in σ in *J. osteosperma*, attesting to the importance of VPD as a driver of plant responses (Novick *et al.*, 2016; Grossiord *et al.*, 2020). As the same drivers were important for hydraulic regulation in the drought-tolerant desert shrub, *Larrea tridentata* (Guo *et al.*, 2020), transient drops in Ψ_{MD} may be strategic only during the wet periods of otherwise water-limited ecosystems, when the reward of carbon uptake exceeds the risk of embolism. In our study, shifts to extreme anisohydry appeared only as responses to discrete monsoon precipitation pulses, suggesting that flexible hydraulic behavior enables *J. osteosperma* to take advantage of soil moisture when available. The responsiveness of hydraulic behavior to soil moisture may explain why, despite similar lateral root densities as pinyon pines (Schwinning *et al.*, 2020), junipers tend to be more physiologically responsive to moderate moisture inputs (Breshears *et al.*, 1997; West *et al.*, 2007; Guo *et al.*, 2018).

The positive relationship between σ and GPP during the monsoon season suggests that temporally-variable hydraulic regulation can maximize carbon uptake during periods of patchy moisture availability. Most interestingly, the timing of σ and GPP indicates that extreme

anisohydry intensifies after GPP peaks. After a precipitation pulse when soil moisture is high, GPP may be immediately stimulated, such that relatively high midday water potentials (low σ) are sufficient to drive water transport along the soil-plant-atmosphere continuum. Because soil moisture declines rapidly after precipitation pulses, extreme anisohydry ($\sigma > 1$) may serve to decrease midday water potentials, maintain water transport in drying soils, and possibly confer a competitive advantage over co-occurring understory species (e.g., Barron-Gafford *et al.*, 2021). The propensity of *Juniperus* spp. to extract soil water even at low soil water potentials (West *et al.*, 2007) is consistent with extreme anisohydry and prolonged elevation of GPP as soils dry.

Possible mechanisms of temporally-varying hydraulic regulation

The mechanisms underlying temporally-varying hydraulic regulation are not well understood, but coordination with other temporally-varying physiology and growth responses could play a role. First, pressure-volume relationships in *Juniperus monosperma* are plastic depending on leaf hydration (Meinzer *et al.*, 2014), such that as a leaf dehydrates, it experiences more negative turgor loss point and less elastic cell walls. Conceivably, stomatal regulation of leaf water potential could also vary with leaf hydration, which may be especially dynamic in evergreen leaves experiencing pulse-driven precipitation. Accounting for plastic adjustment in turgor loss point, *J. monosperma* would ultimately lose turgor at -8.2 MPa (Meinzer *et al.*, 2014), and indeed 99.1% of our *J. osteosperma* Ψ_{MD} observations occurred above this threshold. Temporally-varying leaf-water relations may indicate that osmotic adjustment, cell wall elastic properties, and stomatal regulation could vary in concert to maintain turgor across declining leaf hydration.

Hydraulic regulation strategies could also be linked to temporal dynamics of foliar ABA during soil water stress and recovery (Brodribb & McAdam, 2013). In *Callitris rhomboidea*, sustained water stress led to a decline in ABA such that loss of leaf water potential (and thus guard cell turgor) drove stomatal closure, with the corollary of low ABA also enabling rapid recovery of leaf water potential after rewetting (Brodribb & McAdam, 2013). Among *Cupressaceae*, including *Juniperus* and *Callitris*, the use of leaf desiccation to close stomata during prolonged water stress (Brodribb *et al.*, 2014) could explain why *J. osteosperma* experiences temporally-varying hydraulic regulation. The hydraulic risk of extreme anisohydry could also be partially

compensated by rapid recovery following rewetting, enabling persistence in seasonally dry ecosystems.

Finally, temporally-varying hydraulic regulation may be associated with the timing of belowground dynamics that enable increased conductance, such as fine root and mycorrhizal development (Peek *et al.*, 2006; Lehto & Zwiazek, 2011). In *J. osteosperma*, fine roots grew when soil water was most available and shifted toward deeper layers as the growing season progressed (Peek *et al.*, 2006), and root distributions varied depending on cool-season vs. warm-season precipitation. Rooting dynamics can directly influence plant water potential via rhizosphere conductance, although this is difficult to quantify empirically (Bristow *et al.*, 1984; Sperry *et al.*, 2016). Similarly, mycorrhizal symbionts are known to alter root conductivity (Lehto & Zwiazek, 2011), enhance stomatal conductance (Augé *et al.*, 2015), and increase plant productivity (Mohan *et al.*, 2014), but the temporal dynamics of plant-mycorrhizae relationships under field conditions are poorly understood and merit further investigation (Gehring *et al.*, 2017).

Implications for hydraulic modeling

Plant hydraulic schemes are becoming increasingly represented in vegetation and land surface models (Kennedy *et al.*, 2019b; Eller *et al.*, 2020; Sabot *et al.*, 2020). The link we observed between hydraulic strategy and GPP reinforces the value of these approaches for improved predictions of GPP, especially in dryland ecosystems where patchy resource availability leads to widespread underpredictions of both the magnitude and variability of carbon fluxes (Biedermaier *et al.*, 2017; MacBean *et al.*, 2021b; Barnes *et al.*, 2021). Temporal heterogeneity in plant hydraulic strategy and spatial heterogeneity in topographic characteristics may also interact, as evidenced by high variance in stem Ψ among seven co-located trees (Fig. 1c), and contribute to model underperformance in dryland ecosystems. However, if transient anisohydry does indeed represent a life history strategy to maximize carbon uptake during pulses of moisture availability, then models will need to allow for vegetation hydraulic strategies to vary over time in order to correctly estimate dryland GPP.

One avenue of model development operationalizes the trade-off between carbon gain and hydraulic costs (Sperry *et al.*, 2016; Wolf *et al.*, 2016; Mencuccini *et al.*, 2019), a subset of

stomatal optimization models that accounts for the cavitation risk of low plant Ψ (Wang *et al.*, 2020). Temporally-variable water use strategies may arise as an emergent property of such models (Kannenberg *et al.*, 2022), but likely only where the hydraulic costs of anisohydry and the forfeited carbon gain of isohydry are simultaneously represented. Alternatively, improving the temporal fidelity of optimization models could involve explicit implementation at multiple timescales (daily, weekly) to represent plant physiological acclimation to a changing environment (Joshi *et al.*, 2022). It remains an open question how best to account for transient hydraulic strategies in modeling frameworks, and further research regarding when, where, and how such strategies arise is necessary to evaluate their role in improving estimation of dryland carbon fluxes.

Importance of plant water potential at large scales

In our study of a single growing season, we found that predawn water potential matches the temporal pattern of LUE even more strongly than antecedent soil moisture, which comports with the critical role of water potential to plant physiology. Importantly, predawn water potential improved GPP model fit even though measurement scales varied greatly, with NIRv derived from a 500 m pixel, GPP from a flux tower, and stand water potential averaged from 7 trees within the tower footprint, suggesting that the theoretical foundation connecting plant hydraulics to ecosystem productivity is robust to significant scale mismatch. Inclusion of predawn water potential rather than VPD and soil moisture improved not only model fit of GPP, but also the significantly reduced model bias (Fig. 6), primarily by accounting for the transition between dry season and first monsoon pulse, wherein high predawn water potentials signal physiological readiness for photosynthesis even though vegetation greenness is still lagging. Overprediction of low premonsoon GPP and underprediction of high monsoon GPP were strongly ameliorated by concomitant shifts in predawn water potential.

However, interpreting model residuals as indicative of variations in LUE must be approached with caution, as these residuals also encompass data uncertainty and unaccounted factors. This consideration is particularly important when extrapolating our findings to broader contexts or different temporal scales. Despite these considerations, the substantial improvement of GPP predictions with the inclusion of predawn water potential underscores its promise as a valuable

indicator for capturing intra-annual variability of dryland GPP and warrants additional investigation.

While continuous timeseries of plant water potential remain rare, new technology and collective efforts are poised to increase accessibility to this key metric. At large scales, promising pathways are being explored to develop remote sensing-based proxies of plant water potential using thermal (Farella *et al.*, 2022) and microwave (Konings *et al.*, 2021) observations. Current initiatives to collect and aggregate soil and plant water potential in conjunction with flux tower measurements, including the Ameriflux ‘Year of Water’ and the PSInet Research Coordination Network database, are anticipated to improve water potential data availability and spur synthesis beyond single-site studies. We believe that an expanded network of water potential measurements co-located at existing flux tower sites is essential to calibrate and evaluate both model and remote sensing approaches for estimating productivity.

Conclusions

Though classically considered anisohydric, *J. osteosperma* exhibited multiple hydraulic regulation strategies within a growing season. Extreme anisohydry was only evident after monsoon precipitation pulses, while soils were rapidly drying yet carbon uptake was high. This suggests that temporally flexible hydraulic regulation allows *J. osteosperma* to avoid extreme Ψ_{MD} and xylem cavitation during seasonal drought and prolong high carbon uptake following episodic precipitation events. Furthermore, plant water potential significantly improved GPP model fit and reduced bias despite significant scale mismatch, heralding the immense potential of using plant water stress to increase the temporal fidelity of ecosystem carbon predictions.

Data availability

Data and code are organized as a research compendium in a public GitHub repository (<https://github.com/jessicaguo/juniper-ecodraulics>) and archived on Zenodo (<https://doi.org/10.5281/zenodo.10951221>).

Acknowledgements

The instrumentation for the eddy covariance tower was provided by the AmeriFlux Management Project, administered through the US Department of Energy (DOE). We also thank Newton Tran for assistance with the stem psychrometers, and acknowledge the State of Utah School and Institutional Trust Lands Administration for land permissions. JSG acknowledges support from the US National Science Foundation - Division of Integrative Organismal Biology via a Research Coordination Grant (#2243900). MLB and SAK were supported by the US DOE Environmental System Science program grant #DE-SC0022052. SAK was supported by the US Department of Agriculture (USDA) Forest Service Forest Health Protection Evaluation Monitoring program grant #19-05 and the USDA National Institute of Food and Agriculture Sustainable Agricultural Systems program, grant #2021-68012-35898. MLB and WKS were supported by the NASA SMAP Science Team grant #80NSSC20K1805. WKS and JSG were supported by the NASA Carbon Cycle Science grant #80NSSC23K0109. WRLA acknowledges support from the David and Lucille Packard Foundation, US National Science Foundation grants 1802880, 2003017 and 2044937, and USDA National Institute of Food and Agriculture, Agricultural and Food Research Initiative Competitive Programme, Ecosystem Services and Agro-Ecosystem Management, grant no. 2018-67019-27850.

Author contributions

JSG and SAK conceived of and designed study with input from WRLA. Field data were collected by SAK, processed by SAK and JSG, and analyzed by JSG. Remote sensing data were processed by MLB and analyzed by JSG with input from WKS. JSG prepared the manuscript with input from all co-authors. All authors reviewed the results and approved the final version of the manuscript.

Competing interests

None declared.

References

Ahlström A, Raupach MR, Schurgers G, Smith B, Arneth A, Jung M, Reichstein M, Canadell JG, Friedlingstein P, Jain AK, et al. 2015. The dominant role of semi-arid ecosystems in the trend and variability of the land CO₂ sink. *Science* **348**: 895–899.

Augé RM, Toler HD, Saxton AM. 2015. Arbuscular mycorrhizal symbiosis alters stomatal conductance of host plants more under drought than under amply watered conditions: a meta-analysis. *Mycorrhiza* **25**: 13–24.

Badgley G, Anderegg LDL, Berry JA, Field CB. 2019. Terrestrial gross primary production: Using NIRV to scale from site to globe. *Global Change Biology* **25**: 3731–3740.

Badgley G, Field CB, Berry JA. 2017. Canopy near-infrared reflectance and terrestrial photosynthesis. *Science Advances* **3**: e1602244.

Barnes ML, Farella MM, Scott RL, Moore DJP, Ponce-Campos GE, Biederman JA, MacBean N, Litvak ME, Breshears DD. 2021. Improved dryland carbon flux predictions with explicit consideration of water-carbon coupling. *Communications Earth & Environment* **2**: 1–9.

Barron-Gafford GA, Knowles JF, Sanchez-Cañete EP, Minor RL, Lee E, Sutter L, Tran N, Murphy P, Hamerlynck EP, Kumar P, et al. 2021. Hydraulic redistribution buffers climate variability and regulates grass-tree interactions in a semiarid riparian savanna. *Ecohydrology* **14**: e2271.

Berry JA, Beerling DJ, Franks PJ. 2010. Stomata: Key players in the earth system, past and present. *Current Opinion in Plant Biology* **13**: 232–239.

Biederman JA, Scott RL, Bell TW, Bowling DR, Dore S, Garatuza-Payan J, Kolb TE, Krishnan P, Kroccheck DJ, Litvak ME, et al. 2017. CO₂ exchange and evapotranspiration across dryland ecosystems of southwestern north america. *Global Change Biology* **23**: 4204–4221.

Biederman JA, Scott RL, Goulden ML, Vargas R, Litvak ME, Kolb TE, Yepez EA, Oechel WC, Blanken PD, Bell TW, et al. 2016. Terrestrial carbon balance in a drier world: The effects of water availability in southwestern north america. *Global change biology* **22**: 1867–1879.

Breshears DD, Myers OB, Johnson SR, Meyer CW, Martens SN. 1997. Differential use of spatially heterogeneous soil moisture by two semiarid woody species: *Pinus edulis* and *juniperus monosperma*. *The Journal of Ecology* **85**: 289.

Breshears DD, Myers OB, Meyer CW, Barnes FJ, Zou CB, Allen CD, McDowell NG, Pockman WT. 2009. Tree die-off in response to global change-type drought: Mortality insights from a decade of plant water potential measurements. *Frontiers in Ecology and the Environment* **7**: 185–189.

Bristow KL, Campbell GS, Calissendorff C. 1984. The Effects of Texture on the Resistance to Water Movement within the Rhizosphere. *Soil Science Society of America Journal* **48**: 266–270.

Brodribb TJ, McAdam SAM. 2013. Abscisic acid mediates a divergence in the drought response of two conifers. *Plant Physiology* **162**: 1370–1377.

Brodribb TJ, McAdam SAM, Jordan GJ, Martins SCV. 2014. Conifer species adapt to low-rainfall climates by following one of two divergent pathways. *Proceedings of the National Academy of Sciences* **111**: 14489–14493.

Eller CB, Rowland L, Mencuccini M, Rosas T, Williams K, Harper A, Medlyn BE, Wagner Y, Klein T, Teodoro GS, et al. 2020. Stomatal optimization based on xylem hydraulics (SOX) improves land surface model simulation of vegetation responses to climate. *New Phytologist* **226**: 1622–1637.

Farella MM, Fisher JB, Jiao W, Key KB, Barnes ML. 2022. Thermal remote sensing for plant ecology from leaf to globe. *Journal of Ecology* **110**: 1996–2014.

Feldman AF, Short Gianotti DJ, Konings AG, McColl KA, Akbar R, Salvucci GD, Entekhabi D. 2018. Moisture pulse-reserve in the soil-plant continuum observed across biomes. *Nature Plants* **4**: 1026–1033.

Feng X, Ackerly DD, Dawson TE, Manzoni S, McLaughlin B, Skelton RP, Vico G, Weitz AP, Thompson SE. 2019. Beyond isohydricity: The role of environmental variability in determining plant drought responses. *Plant, Cell & Environment* **42**: 1104–1111.

Garbulsky MF, Peñuelas J, Papale D, Filella I. 2008. Remote estimation of carbon dioxide uptake by a mediterranean forest. *Global Change Biology* **14**: 2860–2867.

Garcia-Forner N, Adams HD, Sevanto S, Collins AD, Dickman LT, Hudson PJ, Zeppel MJ, Jenkins MW, Powers H, Martínez-Vilalta J, et al. 2016a. Responses of two semiarid conifer tree species to reduced precipitation and warming reveal new perspectives for stomatal regulation. *Plant, Cell & Environment* **39**: 38–49.

Garcia-Forner N, Sala A, Biel C, SavÁ© R, Martínez-Vilalta J. 2016b. Individual traits as determinants of time to death under extreme drought in *pinus sylvestris* l. *Tree Physiology* **36**: 1196–1209.

Gehring CA, Swaty RL, Deckert RJ. 2017. Chapter 16 - Mycorrhizas, Drought, and Host-Plant Mortality. In: Johnson NC, Gehring C, Jansa J, eds. Elsevier, 279–298.

Gelfand AE, Ghosh SK. 1998. Model choice: A minimum posterior predictive loss approach. *Biometrika* **85**: 1–11.

Gelman A, Carlin JB, Stern HS, Rubin DB. 2014. *Bayesian data analysis*. Boca Raton, FL, USA: Taylor & Francis.

Gelman A, Rubin DB. 1992. Inference from iterative simulation using multiple sequences. *Statistical Science* **7**: 457–472.

Grantz K, Rajagopalan B, Clark M, Zagona E. 2007. Seasonal shifts in the north american monsoon. *Journal of Climate* **20**: 1923–1935.

Grossiord C, Buckley TN, Cernusak LA, Novick KA, Poulter B, Siegwolf RTW, Sperry JS, McDowell NG. 2020. Plant responses to rising vapor pressure deficit. *New Phytologist* **226**: 1550–1566.

Guo JS, Hultine KR, Koch GW, Kropf H, Ogle K. 2020. Temporal shifts in iso/anisohydry revealed from daily observations of plant water potential in a dominant desert shrub. *New Phytologist* **225**: 713–726.

Guo JS, Hungate BA, Kolb TE, Koch GW. 2018. Water source niche overlap increases with site moisture availability in woody perennials. *Plant Ecology* **219**: 719–735.

Haberstroh S, Lobo-do-Vale R, Caldeira MC, Dubbert M, Cuntz M, Werner C. 2022. Plant invasion modifies isohydricity in mediterranean tree species. *Functional Ecology* **36**: 2384–2398.

Hochberg U, Rockwell FE, Holbrook NM, Cochard H. 2018. Iso/anisohydry: A plantenvironment interaction rather than a simple hydraulic trait. *Trends in Plant Science* **23**: 112–120.

Jones HG. 1998. Stomatal control of photosynthesis and transpiration. *Journal of Experimental Botany* **49**: 387–398.

Joshi J, Stocker BD, Hofhansl F, Zhou S, Dieckmann U, Prentice IC. 2022. Towards a unified theory of plant photosynthesis and hydraulics. *Nature Plants*: 1–13.

Kannenberg SA, Barnes ML, Bowling DR, Driscoll AW, Guo JS, Anderegg WRL. 2023. Quantifying the drivers of ecosystem fluxes and water potential across the soil-plant-atmosphere continuum in an arid woodland. *Agricultural and Forest Meteorology* **329**: 109269.

Kannenberg SA, Driscoll AW, Malesky D, Anderegg WRL. 2021. Rapid and surprising dieback of Utah juniper in the southwestern USA due to acute drought stress. *Forest Ecology and Management* **480**: 118639.

Kannenberg SA, Guo JS, Novick KA, Anderegg WRL, Feng X, Kennedy D, Konings AG, Martínez-Vilalta J, Matheny AM. 2022. Opportunities, challenges and pitfalls in characterizing plant water-use strategies. *Functional Ecology* **36**: 24–37.

Kennedy D, Swenson S, Oleson KW, Lawrence DM, Fisher R, Lola da Costa AC, Gentile P. 2019a. Implementing Plant Hydraulics in the Community Land Model, Version 5. *Journal of Advances in Modeling Earth Systems* **11**: 485–513.

Kennedy D, Swenson S, Oleson KW, Lawrence DM, Fisher R, Lola da Costa AC, Gentile P. 2019b. Implementing Plant Hydraulics in the Community Land Model, Version 5. *Journal of Advances in Modeling Earth Systems* **11**: 485–513.

King DA, Turner DP, Ritts WD. 2011. Parameterization of a diagnostic carbon cycle model for continental scale application. *Remote Sensing of Environment* **115**: 1653–1664.

Klein T. 2014. The variability of stomatal sensitivity to leaf water potential across tree species indicates a continuum between isohydric and anisohydric behaviours (S Niu, Ed.). *Functional Ecology* **28**: 1313–1320.

Konings AG, Saatchi SS, Frankenberg C, Keller M, Leshyk V, Anderegg WRL, Humphrey V, Matheny AM, Trugman A, Sack L, et al. 2021. Detecting forest response to droughts with global observations of vegetation water content. *Global Change Biology* **27**: 6005–6024.

Lehto T, Zwiazek JJ. 2011. Ectomycorrhizas and water relations of trees: a review. *Mycorrhiza* **21**: 71–90.

Linton MJ, Sperry JS, Williams DG. 1998. Limits to water transport in *juniperus osteosperma* and *pinus edulis*: Implications for drought tolerance and regulation of transpiration. *Functional Ecology* **12**: 906–911.

Loik ME, Breshears DD, Lauenroth WK, Belnap J. 2004. A multi-scale perspective of water pulses in dryland ecosystems: Climatology and ecohydrology of the western USA. *Oecologia* **141**: 269–281.

MacBean N, Scott RL, Biederman JA, Peylin P, Kolb T, Litvak ME, Krishnan P, Meyers TP, Arora VK, Bastrikov V, et al. 2021a. Dynamic global vegetation models underestimate net CO₂ flux mean and inter-annual variability in dryland ecosystems. *Environmental Research Letters* **16**: 094023.

MacBean N, Scott RL, Biederman JA, Peylin P, Kolb T, Litvak ME, Krishnan P, Meyers TP, Arora VK, Bastrikov V, et al. 2021b. Dynamic global vegetation models underestimate net CO₂ flux mean and inter-annual variability in dryland ecosystems. *Environmental Research Letters* **16**: 094023.

Martínez-Vilalta J, Poyatos R, Aguadé D, Retana J, Mencuccini M. 2014. A new look at water transport regulation in plants. *New Phytologist* **204**: 105–115.

Martínez-Vilalta J, Santiago LS, Poyatos R, Badiella L, de Cáceres M, Aranda I, Delzon S, Vilagrosa A, Mencuccini M. 2021. Towards a statistically robust determination of minimum water potential and hydraulic risk in plants. *New Phytologist* **232**: 404–417.

McDowell N, Pockman WT, Allen CD, Breshears DD, Cobb N, Kolb T, Plaut J, Sperry J, West A, Williams DG, et al. 2008. Mechanisms of plant survival and mortality during drought: Why do some plants survive while others succumb to drought? *New Phytologist* **178**: 719–739.

Meinzer FC, Woodruff DR, Marias DE, McCulloh KA, Sevanto S. 2014. Dynamics of leaf water relations components in co-occurring iso- and anisohydric conifer species. *Plant, Cell & Environment* **37**: 2577–2586.

Mencuccini M, Manzoni S, Christoffersen B. 2019. Modelling water fluxes in plants: from tissues to biosphere. *New Phytologist* **222**: 1207–1222.

Mohan JE, Cowden CC, Baas P, Dawadi A, Frankson PT, Helmick K, Hughes E, Khan S, Lang A, Machmuller M, et al. 2014. Mycorrhizal fungi mediation of terrestrial ecosystem responses to global change: mini-review. *Fungal Ecology* **10**: 3–19.

Monteith JL. 1972. Solar radiation and productivity in tropical ecosystems. *Journal of Applied Ecology* **9**: 747–766.

Monteith JL, Moss CJ, Cooke GW, Pirie NW, Bell GDH. 1977. Climate and the efficiency of crop production in britain. *Philosophical Transactions of the Royal Society of London. B, Biological Sciences* **281**: 277–294.

Moritz S, Bartz-Beielstein T. 2017. imputeTS: Time series missing value imputation in r. *R J.* **9**: 207.

Nolan RH, Tarin T, Santini NS, McAdam SAM, Ruman R, Eamus D. 2017. Differences in osmotic adjustment, foliar abscisic acid dynamics, and stomatal regulation between an isohydric and anisohydric woody angiosperm during drought. *Plant, Cell & Environment* **40**: 3122–3134.

Novick KA, Ficklin DL, Baldocchi D, Davis KJ, Ghezzehei TA, Konings AG, MacBean N, Raoult N, Scott RL, Shi Y, et al. 2022. Confronting the water potential information gap. *Nature Geoscience* **15**: 158–164.

Novick KA, Ficklin DL, Stoy PC, Williams CA, Bohrer G, Oishi A, Papuga SA, Blanken PD, Noormets A, Sulman BN, et al. 2016. The increasing importance of atmospheric demand for ecosystem water and carbon fluxes. *Nature Climate Change* **6**: 1023.

Novick KA, Konings AG, Gentine P. 2019. Beyond soil water potential: An expanded view on isohydricity including land–atmosphere interactions and phenology. *Plant, Cell & Environment* **42**: 1802–1815.

Noy-Meir I. 1973. Desert ecosystems: Environment and producers. *Annual Review of Ecology and Systematics* **4**: 25–51.

Ogle K, Barber JJ, Barron-Gafford GA, Bentley LP, Young JM, Huxman TE, Loik ME, Tissue DT. 2015. Quantifying ecological memory in plant and ecosystem processes. *Ecology Letters* **18**: 221–235.

Ogle K, Reynolds JF. 2004. Plant responses to precipitation in desert ecosystems: Integrating functional types, pulses, thresholds, and delays. *Oecologia* **141**: 282–294.

Peek MS, Leffler AJ, Hipps L, Ivans S, Ryel RJ, Caldwell MM. 2006. Root turnover and relocation in the soil profile in response to seasonal soil water variation in a natural stand of utah juniper (*juniperus osteosperma*). *Tree Physiology* **26**: 1469–1476.

Pierrat Z, Nehemy MF, Roy A, Magney T, Parazoo NC, Laroque C, Pappas C, Sonnentag O, Grossmann K, Bowling DR, et al. 2021. Tower-based remote sensing reveals mechanisms behind a two-phased spring transition in a mixed-species boreal forest. *Journal of Geophysical Research: Biogeosciences* **126**: e2020JG006191.

Plaut JA, Yepez EA, Hill J, Pangle R, Sperry JS, Pockman WT, McDowell NG. 2012. Hydraulic limits preceding mortality in a piñonjuniper woodland under experimental drought. *Plant, Cell & Environment* **35**: 1601–1617.

Plummer M. 2003. Proceedings of the 3rd international workshop on distributed statistical computing. In: Vienna, Austria.

Plummer M. 2022. *Rjags: Bayesian graphical models using MCMC*.

Poulter B, Frank D, Ciais P, Myneni RB, Andela N, Bi J, Broquet G, Canadell JG, Chevallier F, Liu YY. 2014. Contribution of semi-arid ecosystems to interannual variability of the global carbon cycle. *Nature* **509**: 600–603.

R Core Team. 2021. *R: A language and environment for statistical computing*. Vienna, Austria: R Foundation for Statistical Computing.

Running SW, Nemani RR, Heinsch FA, Zhao M, Reeves M, Hashimoto H. 2004. A continuous satellite-derived measure of global terrestrial primary production. *Bioscience* **54**: 547–560.

Sabot MEB, De Kauwe MG, Pitman AJ, Medlyn BE, Ellsworth DS, Martin-StPaul NK, Wu J, Choat B, Limousin J-M, Mitchell PJ, et al. 2022. One stomatal model to rule them all? Toward improved representation of carbon and water exchange in global models. *Journal of Advances in Modeling Earth Systems* **14**: e2021MS002761.

Sabot MEB, De Kauwe MG, Pitman AJ, Medlyn BE, Verhoeef A, Ukkola AM, Abramowitz G. 2020. Plant profit maximization improves predictions of european forest responses to drought. *New Phytologist* **226**: 1638–1655.

Schwinning S, Litvak ME, Pockman WT, Pangle RE, Fox AM, Huang C-W, McIntire CD. 2020. A 3-dimensional model of *Pinus edulis* and *Juniperus monosperma* root distributions in New Mexico: implications for soil water dynamics. *Plant and Soil* **450**: 337–355.

Smith WK, Dannenberg MP, Yan D, Herrmann S, Barnes ML, Barron-Gafford GA, Biederman JA, Ferrenberg S, Fox AM, Hudson A, et al. 2019. Remote sensing of dryland ecosystem structure and function: Progress, challenges, and opportunities. *Remote Sensing of Environment* **233**: 111401.

Sperry JS, Wang Y, Wolfe BT, Mackay DS, Anderegg WRL, McDowell NG, Pockman WT. 2016. Pragmatic hydraulic theory predicts stomatal responses to climatic water deficits. *New Phytologist* **212**: 577–589.

Tardieu F, Simonneau T. 1998. Variability among species of stomatal control under fluctuating soil water status and evaporative demand: Modelling isohydric and anisohydric behaviours. *Journal of Experimental Botany* **49**: 419–432.

Vines S, Gilks W, Wild P. 1996. Fitting bayesian multiple random effects models. *Statistics and Computing* **6**: 337–346.

Wang X, Biederman JA, Knowles JF, Scott RL, Turner AJ, Dannenberg MP, Köhler P, Frankenberg C, Litvak ME, Flerchinger GN, et al. 2022. Satellite solar-induced chlorophyll fluorescence and near-infrared reflectance capture complementary aspects of dryland vegetation productivity dynamics. *Remote Sensing of Environment* **270**: 112858.

Wang Y, Sperry JS, Anderegg WRL, Venturas MD, Trugman AT. 2020. A theoretical and empirical assessment of stomatal optimization modeling. *New Phytologist* **227**: 311–325.

West AG, Hultine KR, Jackson TL, Ehleringer JR. 2007. Differential summer water use by *pinus edulis* and *juniperus osteosperma* reflects contrasting hydraulic characteristics. *Tree Physiology* **27**: 1711–1720.

Williams AP, Cook BI, Smerdon JE. 2022. Rapid intensification of the emerging southwestern North American megadrought in 20202021. *Nature Climate Change* **12**: 232–234.

Wolf A, Anderegg WRL, Pacala SW. 2016. Optimal stomatal behavior with competition for water and risk of hydraulic impairment. *Proceedings of the National Academy of Sciences* **113**: E7222–E7230.

Wu G, Guan K, Li Y, Novick KA, Feng X, McDowell NG, Konings AG, Thompson SE, Kimball JS, De Kauwe MG. 2021. Interannual variability of ecosystem iso/anisohydry is regulated by environmental dryness. *New Phytologist* **229**: 2562–2575.

Yuan W, Liu S, Zhou G, Zhou G, Tieszen LL, Baldocchi D, Bernhofer C, Gholz H, Goldstein AH, Goulden ML, et al. 2007. Deriving a light use efficiency model from eddy covariance flux data for predicting daily gross primary production across biomes. *Agricultural and Forest Meteorology* **143**: 189–207.

Zeng Y, Hao D, Huete A, Dechant B, Berry J, Chen JM, Joiner J, Frankenberg C, Bond-Lamberty B, Ryu Y, et al. 2022. Optical vegetation indices for monitoring terrestrial ecosystems globally. *Nature Reviews Earth & Environment* **3**: 477–493.

Zhang Y, Song C, Sun G, Band LE, Noormets A, Zhang Q. 2015. Understanding moisture stress on light use efficiency across terrestrial ecosystems based on global flux and remote-sensing data. *Journal of Geophysical Research: Biogeosciences* **120**: 2053–2066.

Zhao M, Running SW. 2010. Drought-induced reduction in global terrestrial net primary production from 2000 through 2009. *Science* **329**: 940–943.

Supporting Information

Fig. S1 Model fit of Ψ_{MD}

Fig. S2 Antecedent weights of soil moisture for two GPP residual models

Figure legends

Figure 1: Daily time series of site-level environmental conditions, plant water potential of *Juniperus osteosperma*, and gross primary productivity, (a) maximum vapor pressure deficit (D) and photosynthetically active radiation (PAR), (b) mean air temperature (T_{air}), volumetric water content (VWC) at 5 cm and 10 cm, and total precipitation (black bars), (c) chamber and automated daily measurements of mean stem water potential, and (d) total gross primary productivity (GPP). Labeled boxes subdivide the study period into premonsoon, monsoon, and fall seasons; error bars represent population standard deviation

Figure 2: Midday (Ψ_{MD}) vs. predawn (Ψ_{PD}) stem water potential of *Juniperus osteosperma* in each season. Points are colored by the mean daily volumetric water content at 10 cm (W_{10}). Solid line is the 1:1 line. Dashed lines represent linear fits by season, with a segmented regression joined at Ψ_{PD} of -0.6 MPa during the monsoon season

Figure 3: Coefficients estimated by the hydraulic regulation model (Eqn. 3 – 6) that linearly relates Ψ_{MD} to Ψ_{PD} , where the slope (σ) and intercept (λ) vary with antecedent environmental variables D^{ant} and W_{10}^{ant} . Posterior mean and 95% credible interval (CI) of the (a) covariate effects on σ and λ and (b) antecedent weights ω associated with covariates D and W_{10} . Gray horizontal lines indicate the prior means, asterisks indicate significant covariate effects, and error bars represent the 95% CIs

Figure 4: Comparison of the predicted slope σ , representing the stringency of hydraulic regulation, to gross primary productivity (GPP) over the study period, including (a) a daily time series across three seasons, (b) bivariate plots by season, and (c) Pearson's correlation coefficient (estimate and 95% confidence interval) during monsoon season across a range of daily offsets where GPP leads σ . The predicted slope σ is represented by the posterior mean and 95% credible interval from the hydraulic regulation model (Eqn. 3 – 6). Solid line in (b) represents a significant linear relationship between σ and GPP during the monsoon season

Figure 5: To account for the light use constraints on gross primary productivity (GPP), GPP is modeled as a function of near infrared reflectance of vegetation (NIRv) and photosynthetically active radiation (PAR), including (a) a time series of GPP with scaled values of NIRv and PAR,

(b) posterior mean and 95% credible interval (CI) of the covariate effects, and (c) predicted versus observed GPP from the initial GPP model (Eqn. 7, 8). Gray horizontal lines indicate the prior means, asterisks indicate significant covariate effects, error bars represent the 95% CIs, the solid diagonal is the 1:1 line, and the dashed line represents the line of best fit

Figure 6: To evaluate the hydraulic constraints on GPP after light use is accounted for, GPP residuals (observed GPP minus modeled GPP) were modeled with three sets of covariates: vapor pressure deficit and soil water content ('Env', Eqn. 5 & Eqn. 10), soil water content ('Soil only', Eqn. 5 & Eqn. 11), and site-averaged predawn water potential (' Ψ only', Eqn. 12). Model inputs are shown as (a) time series of daily GPP residuals with daily maximum vapor pressure deficit (D), volumetric water content at 10 cm (W_{10}), and site-averaged predawn water potential ($\overline{\Psi_{PD}}$), all standardized to the same scale. Posterior mean and 95% credible interval (CI) of the (b) covariate effects and (c) predicted versus observed residuals from the 'Env', 'Soil only', and ' Ψ only' models. Gray horizontal lines indicate the prior means, asterisks indicate significant covariate effects, error bars represent the 95% CIs, the solid diagonal is the 1:1 line, and the dashed line represents the line of best fit. Model comparison statistics of effective number of parameters (pD) and posterior predictive loss ($D\infty$) are shown in (b), wherein lower values indicate better predictive performance

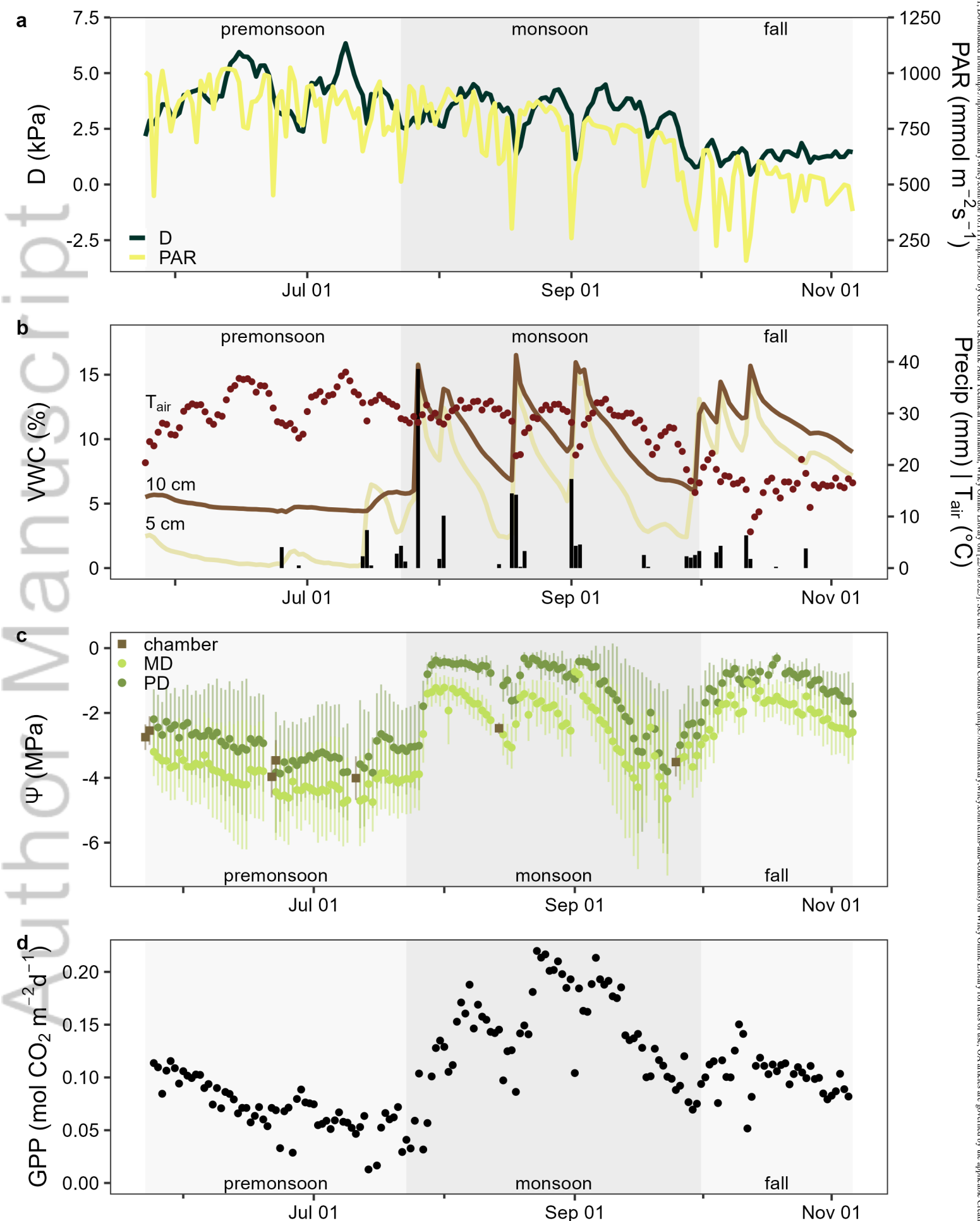


Fig. 1.png

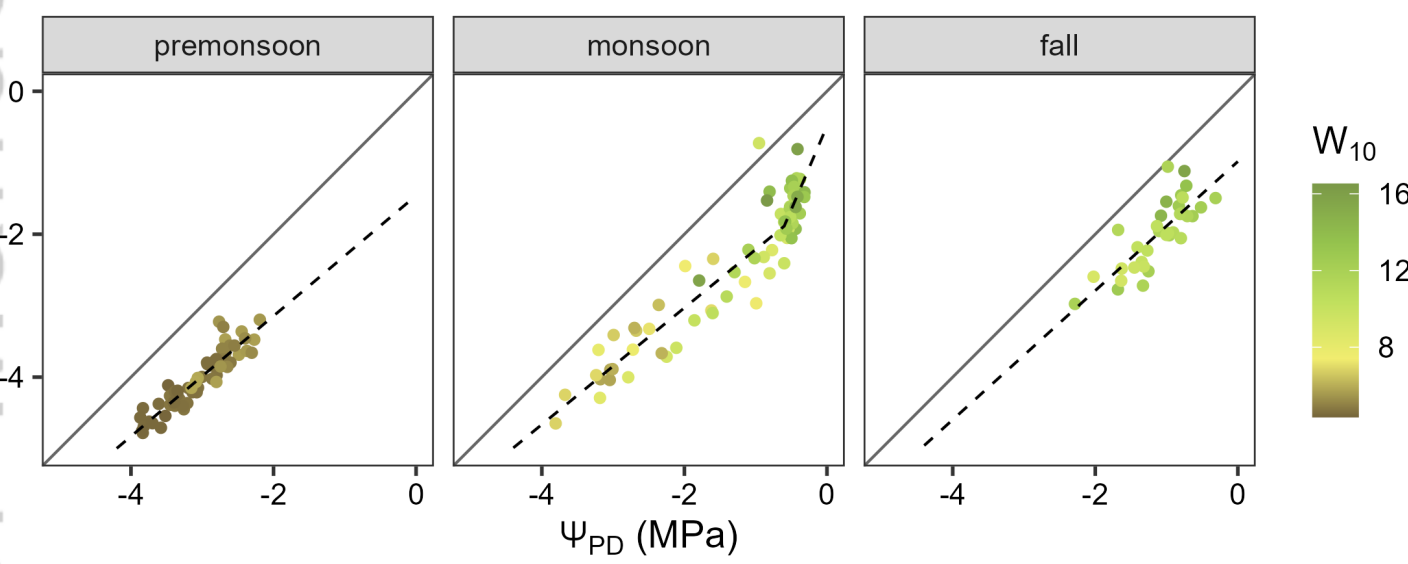
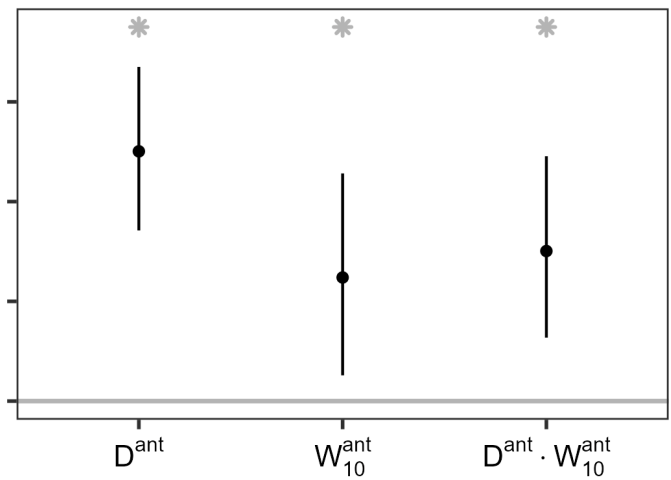
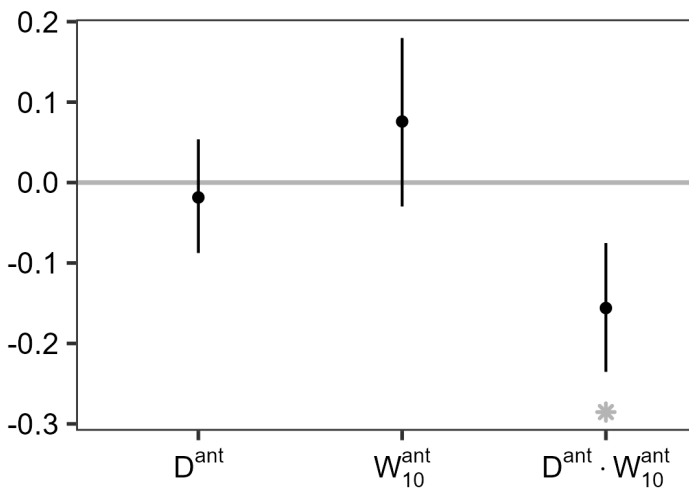


Fig. 2.png

a

 σ  λ 

b

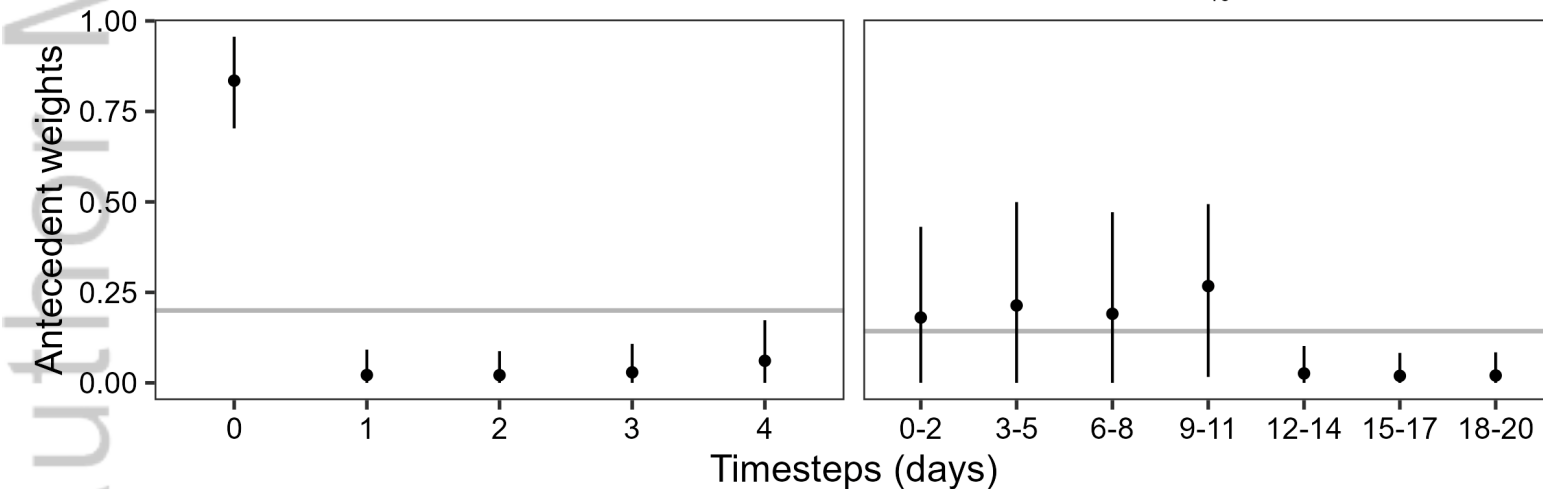
 D^{ant} W_{10}^{ant} 

Fig. 3.png

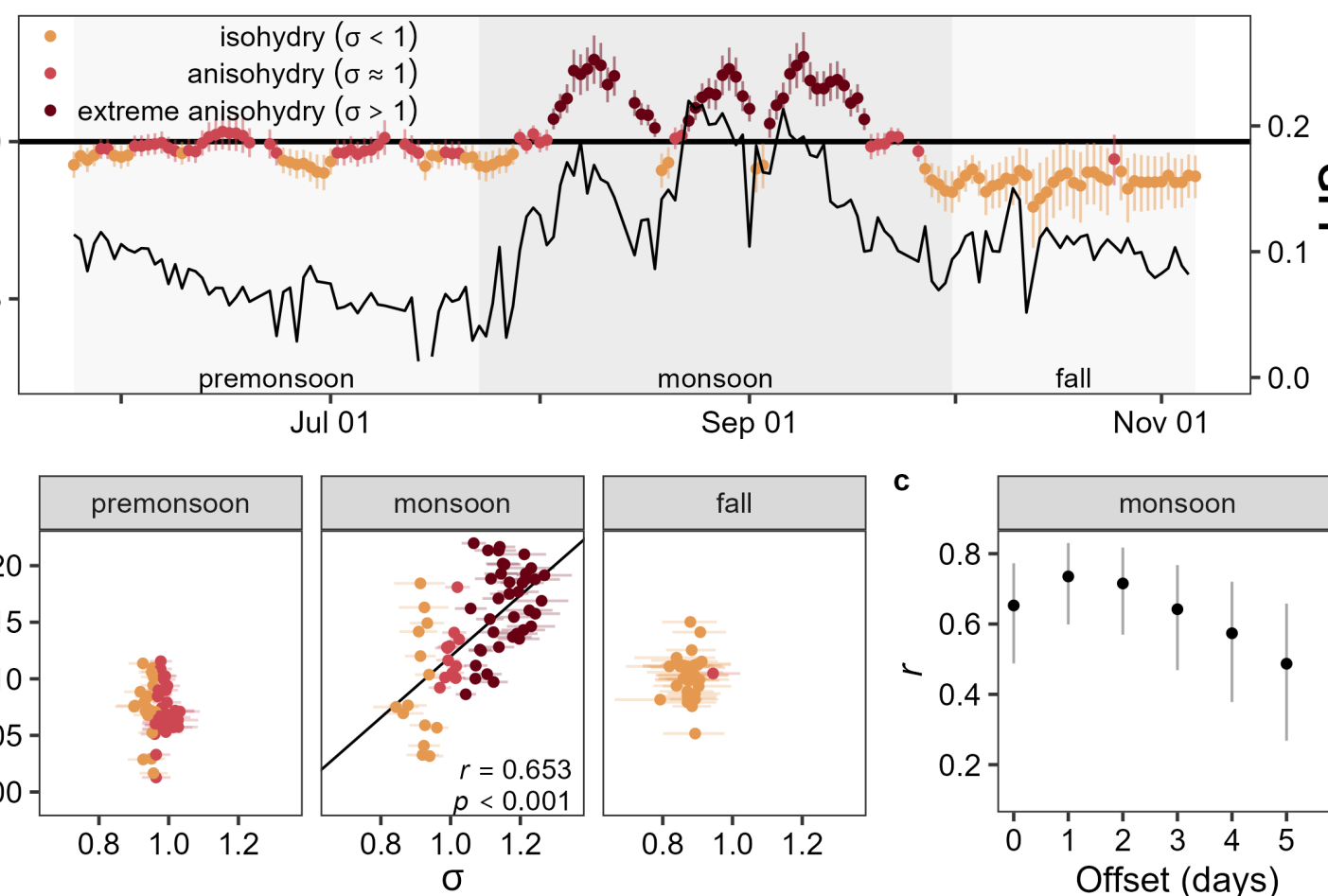


Fig. 4.png

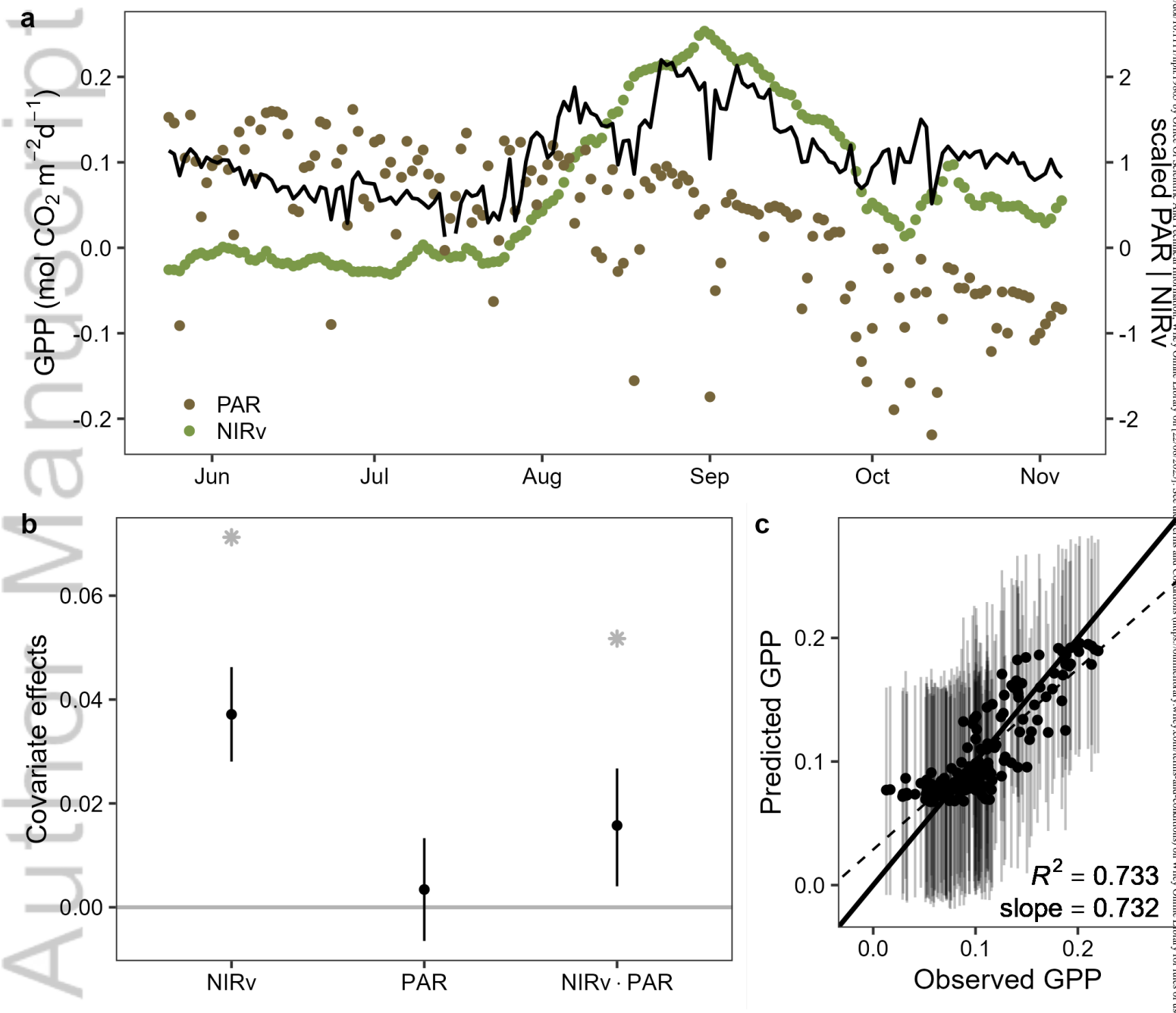


Fig. 5.png

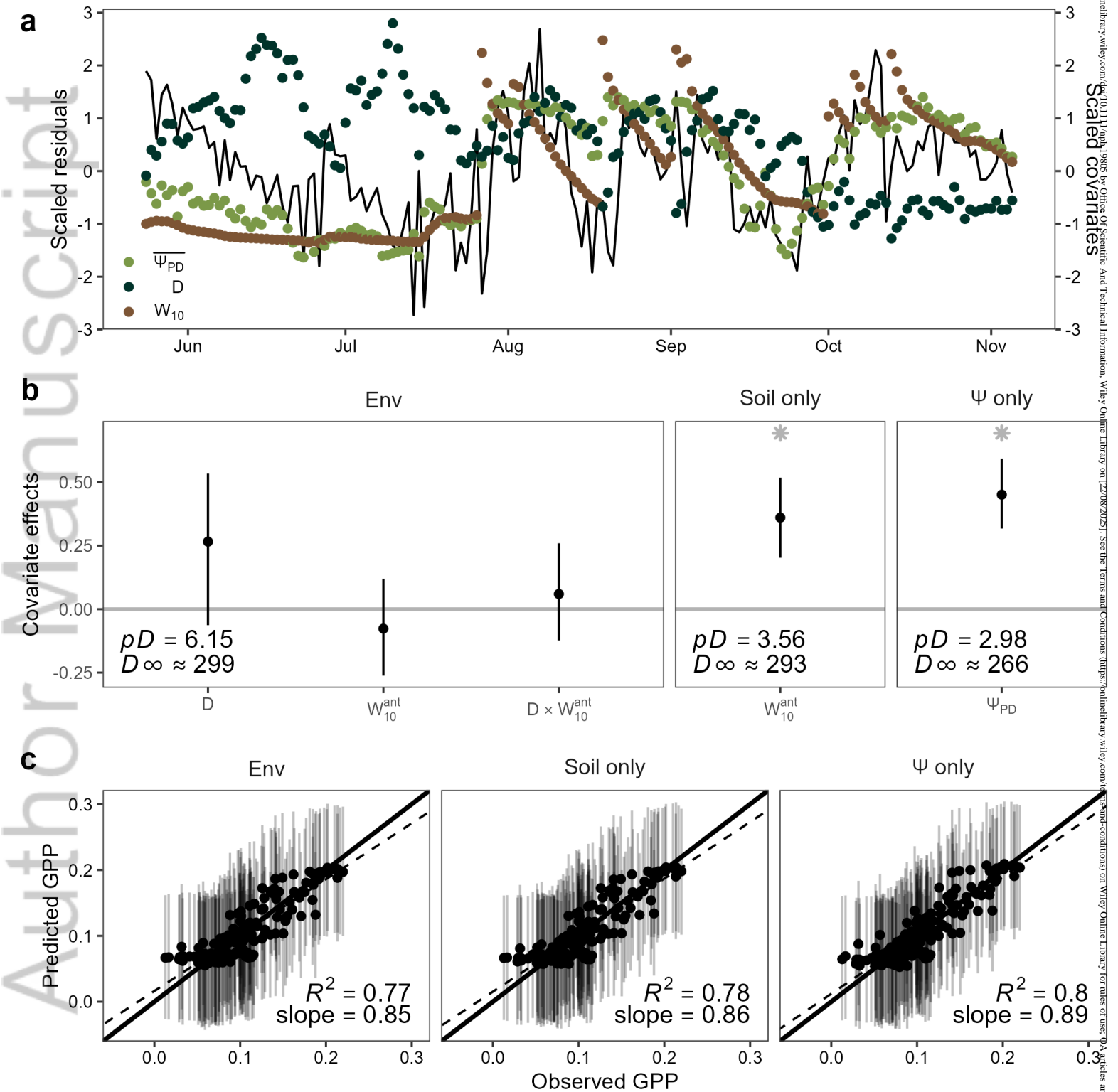


Fig. 6.png